Biosensors and Bioelectronics 139 (2019) 111327

Contents lists available at ScienceDirect

Biosensors and Bioelectronics

journal homepage: www.elsevier.com/locate/bios

Hierarchical Cu@Cu_xO nanowires arrays-coated gold nanodots as a highly sensitive self-supported electrocatalyst for L-cysteine oxidation

Huu Tuan Le[a], Duy Thanh Tran[a], Thi Luu Luyen Doan[a], Nam Hoon Kim[a,*], Joong Hee Lee[a,b,**]

[a] Advanced Materials Institute of BIN Convergence (BK21 Plus Global), Department of BIN Convergence Technology, Chonbuk National University, Jeonju, Jeonbuk, 54896, Republic of Korea

[b] Center for Carbon Composite Materials, Department of Polymer & Nano Science and Technology, Chonbuk National University, Jeonju, Jeonbuk, 54896, Republic of Korea

ARTICLE INFO

Keywords:
Copper-copper oxide nanowires
Gold nanoparticle layer
Electrocatalyst
Electrochemical biosensor

ABSTRACT

The sensitivity, selectivity, and stability of an electrochemical sensor for detecting small biomolecules can be significantly upgraded through properly controlling the morphology and chemical structure of electrocatalyst. Herein, we fabricated a unique hierarchical nanostructure based on Cu@Cu_xO nanowires (NWs) array uniformly depositing with a layer of gold nanoparticles (2–3 nm) through a simple electroless deposition process. The Au–Cu@Cu_xO NWs hybrid was successfully applied as a novel binder-free self-supported biosensor towards L-cysteine detection with low limit of detection (1.25 μM), wide linear detection range (1.25 μM–1.94 mM), long-term stability (four weeks), and excellent selectivity. In addition, the hybrid-based sensor accurately detected L-cysteine in real samples. It was found that the obtained nanostructure with the formation of strong interaction between Au and Cu phase produces synergistic effects, which improve exposed electroactive site number, accelerate charge transfer rate, and increase surface area, thereby boosting the sensing performance. The results open a potential way to develop electrochemical sensor for efficiently detecting not only L-cysteine but also other small molecules with high sensitivity, accuracy, stability, and cost-effectiveness in health care and disease diagnosis.

1. Introduction

In recent years, the development of electrochemical biosensors for food quality controlling, environmental monitoring, health care, and clinical diagnostics, has become a hot topic due to their ease of synthesis, low cost, fast response, reliability, and suitability for direct analyses. Owning to unique morphology, structure, and properties, metal nanomaterials have important role in producing efficient electrochemical biosensors with enhanced sensitivity and long-term stability (Jana et al., 2018; Karmaoui et al., 2017; Thanh et al., 2018). Among various metal nanomaterials having high catalytic activity, good stability, abundant availability, and low cost, Cu-based nanostructures derived from Cu and copper oxides have been widely and successfully used (Billy and Co, 2018; Mierczynski et al., 2016). Mean Cu metal has been considered as the most common connector with excellent electrical conductivity for creating electronic nanodevices (Jason et al., 2016; Liang et al., 2019), Cu_xO semiconductor catalyst with a narrow band gap of 1.2–1.7 eV and physicochemical stability has been employed for diverse catalytic synthesis due to the partially filled d-orbitals from the Cu ion and the effect of the oxide ligand field on such partially filled d-orbitals (Gawande et al., 2012). Therefore, Cu-Cu_xO materials have exhibited interesting behaviors for electrocatalysis (Eilert et al., 2017; Huan et al., 2017). The properties of these nanomaterials have been demonstrated to be highly dependent on size and morphology; therefore, proper synthesis and applications of well-defined Cu_xO-Cu nanostructures with specific morphology, such as nanoparticles, nanoneedles, nanoribbons, nanosheets, and dendrites have been proposed (Peng et al., 2016; Ren et al., 2017). Needle nanostructures have been found to have high potential with many advantages over others, such as uniformity, large surface area, abundantly active site numbers, and easy synthesis (Li et al., 2017; Momeni et al., 2016). In particular, directly coupling them with a three-dimensional foam (3DF) structure can further enhance electrocatalytic activity, surface area, charge transfer, and stability (Liu et al., 2017; Wang et al., 2017).

* Corresponding author.
** Corresponding author. Advanced Materials Institute of BIN Convergence (BK21 Plus Global), Department of BIN Convergence Technology, Chonbuk National University, Jeonju, Jeonbuk, 54896, Republic of Korea.
E-mail addresses: nhk@chonbuk.ac.kr (N.H. Kim), jhl@chonbuk.ac.kr (J.H. Lee).

https://doi.org/10.1016/j.bios.2019.111327
Received 13 March 2019; Received in revised form 29 April 2019; Accepted 14 May 2019
Available online 15 May 2019
0956-5663/

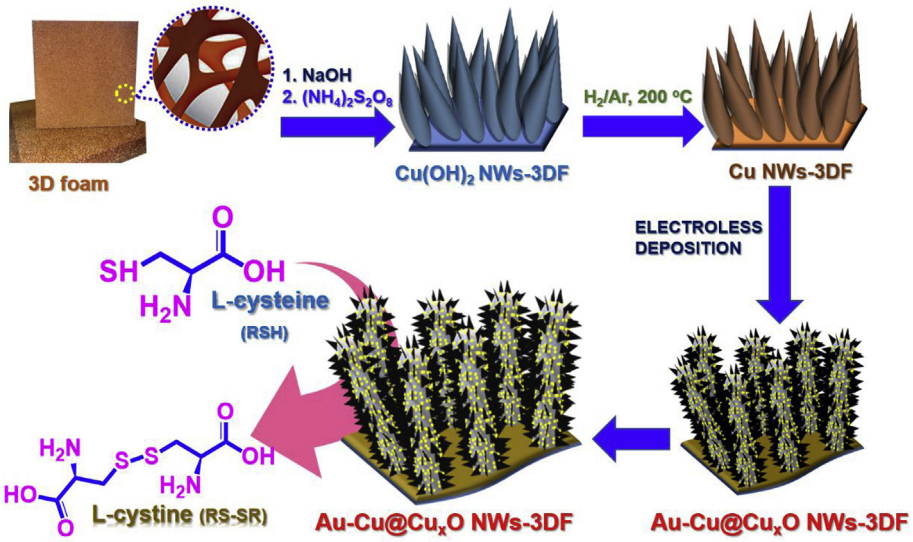

Scheme 1. Schematic illustration for fabrication of Au–Cu@Cu_xO NWs-3DF hybrid.

Recent development in electrocatalysis have indicated that the merging of a noble metal with a transition metal or its oxide phases (or both) into closely coupled heterostructure can impressively result in the alteration of catalytic activity, selectivity, and stability (Tran et al., 2019; Yang et al., 2017). In this context, gold (Au) has shown very promising catalytic performance and efficiencies because of its unique geometric and electronic structures (Ulrich et al., 2018; Zhao et al., 2017). The hybridization of noble metal, such as Au nanomaterial, with Cu-based catalysts can alter geometry, morphology, structure of resulting materials, and then the Cu-Cu_xO surface ratio, which is evidenced as an important factor for the catalytic activity (Caldas et al., 2017; Konar et al., 2016). In addition, the formation of high interaction between Au–Cu effectively modulates electronic features and surface chemistry of semiconducting catalyst with more electroactive sites for the enhanced catalytic process (Tran et al., 2019). Furthermore, the reaction kinetic can be greatly accelerated because the presence of an Au layer at Cu-Cu_xO boundary regions can efficiently improve hetero-conductivity between Cu substrate and non-conductive Cu_xO catalyst. For instance, Mishara et al. explored an enhancement of conductivity, accelerated electron transfer, and catalytic properties of a nanocomposite based on CuO nanostructures and Au (Mishra et al., 2019). Some other previous reports (Abad et al., 2005; Yu et al., 2010) also demonstrated that the combination of noble metal with Cu-Cu_xO hybrid not only display superior physicochemical behaviors but also better catalytic activity and stability. Therefore, it is expected that a unique hybridization of Au nanocrystals with the Cu-Cu_xO nanoneedles on a 3DF may be a promising way to enhance the catalytic efficiency of electrochemical sensor.

L-cysteine (L-cys), an α-amino acid, plays a crucial role in biological systems as well as in food processing and medical production (Deng et al., 2009; Silva et al., 2013). This substance is important for metabolizing essential biochemicals. It has been applied as a radioprotective agent, a free radical scavenger, and a cancer indicator (Zhou et al., 2007). In addition, L-cys has also been added into antibiotic drugs for treatment of skin damages, and it has been utilized as an antioxidant in food production (Majd et al., 2013). Therefore, the sensitive and selective determination of L-cys is very important in biochemistry, pharmaceuticals, and clinical analysis. Some efforts have developed electrochemical sensors for L-cys detection (Sornambikai et al., 2017; Wang et al., 2015). Although enzymatic sensors have been commonly applied (Hassan et al., 2007; Singh et al., 2017), the high cost and unstable nature of enzymes are critical issues hindering sensor's practical applications (Ghanbari and Babaei, 2016; Wang et al., 2018). Another problem is that the use of polymer binder significantly reduces the charge transfer rate, obstruct the catalytic active sites, and prohibit electrolyte/reactant diffusion. In addition, the aggregation and dissolution of catalyst during the electrochemical operation significantly decrease catalytic activity, reproducibility, and stability. To address these issues, we developed a novel nanoarchitecture based on Au nanocrystals (2–3 nm) an a complex 1D Cu@Cu_xO nanowires arrays on 3DF. The synergistic effects from high interaction between Au–Cu provided more exposed active sites, large surface area, and good conductivity, thereby yielding outstanding catalytic behavior towards L-cys detection.

2. Experimental

2.1. Synthesis of $Cu(OH)_2$ NWs-3DF

In a typical synthesis procedure, 3D copper foam (3DF) was cut into 1 cm × 5 cm slice and cleaned by dipping for 15 min (with the help of sonication) in acetone, ethanol, and acetic acid in sequence. Then the 3DF was washed quickly with water until a pH of 7 was achieved. The resulting 3DF was then immersed in a mixture containing of 2.5 M NaOH and 0.13 M $(NH_4)_2S_2O_8$ at room temperature and gently stirred for 15 min. After the $Cu(OH)_2$ nanoneedle arrays were uniformly grown on the 3DF, the sample was washed with water until a pH of 7 was achieved followed by drying at 60 °C for 12 h.

2.2. Synthesis of Au–Cu@Cu_xO NWs-3DF

For preparing the Au–Cu@Cu_xO NWs-3DF hybrid, the $Cu(OH)_2$ NWs-3DF was firstly reduced to Cu NWs-3DF at 200 °C in a flow of Ar gas (100 sccm) and H_2 gas (50 sccm) for 80 min. A heating rate of 3 °C·min^{-1} was used to increase temperature to reaction condition. After the reaction finished, the system was fast cooled to room temperature under Ar flow (100 sccm). Subsequently, the sample was removed and immediately immersed in 1 mM $HAuCl_4$ solution for 1 min to allow Au electroless depositing on sample (Scheme 1). The obtained Au–Cu@Cu_xO NWs-3DF was carefully washed with water before being dried under a flow of N_2 gas.

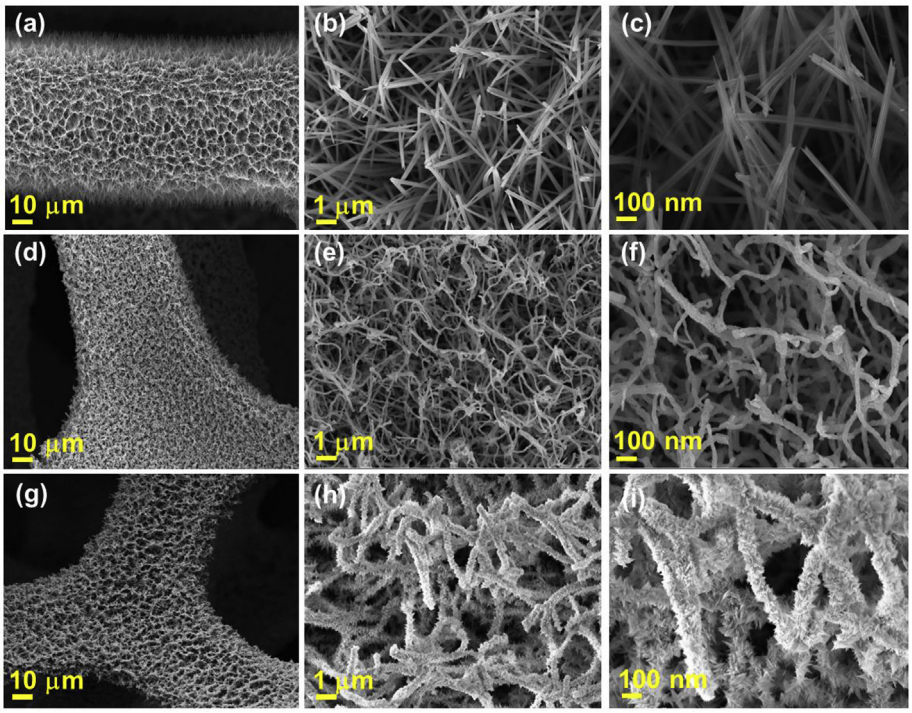

Fig. 1. SEM images at different magnifications of (a–c) $Cu(OH)_2$ NWs-3DF; (d–f) Cu NWs-3DF; and (g–i) Au–Cu@Cu_xO NWs-3DF hybrid.

3. Results and discussion

3.1. Morphological studies

Scheme 1 shows the fabrication strategy of the Au–Cu@Cu_xO NWs-3DF hybrid. In this context, 3DF was first oxidized to produce Cu^{2+} ions, which were then converted to uniform $Cu(OH)_2$ NWs, well attaching on the skeleton surface of 3DF due to the simultaneous effect of oxidant agent ($(NH_4)_2S_2O_8$) and base (NaOH) (Kar et al., 2017). A reduction process of $Cu(OH)_2$ NWs in H_2 at 200 °C for 80 min generated Cu NNs, which were then converted to the Au–Cu@Cu_xO NWs-3DF through a subsequent galvanic reaction and oxidation process during immersion in the Au precursor (Thanh et al., 2016). FE-SEM was used to evaluate the typical morphology and structure of the $Cu(OH)_2$ NWs-3DF, Cu NWs-3DF, and Au–Cu@Cu_xO NWs-3DF materials. Fig. 1a shows FE-SEM image of the $Cu(OH)_2$ NWs-3DF hybrid with a uniform and porous structure. The skeleton surface of 3DF is completely covered by $Cu(OH)_2$ nanoneedle arrays with the diameter in the range from 70 to 80 nm (Fig. 1b and c). In the case of the Cu NWs-3DF hybrid, the uniform and porous characteristics are similar to that of the $Cu(OH)_2$ NNs-3DF (Fig. 1d). However, the Cu NNs displays interconnected flexibility and a rough surface, suggesting a better porosity than Cu $(OH)_2$ NWs-3DF (Fig. 1e and f). Particularly, the Au–Cu@Cu_xO NWs-3DF hybrid exhibits an extremely rough and highly porous morphology on the skeleton surface of the 3DF (Fig. 1g). In this regard, the Cu nanoneedles are thoroughly coated with vertical layer-like Cu_xO nanostructures to create uniform hetero-nanobrush architecture (Fig. 1h and i). Such obtained characteristics can result in a highly porous feature and large specific surface area with the enhanced active site number, flexible, short, and diverse channels for the mass transfer and ion diffusion, and improved interfacial contact area, promising with regard to its use for electrochemical reactions.

TEM analysis was used to characterize the insight into nanostructure of the Au–Cu@Cu_xO NWs. The typical morphology of the Au–Cu@Cu_xO NWs exhibited a Cu nanoneedle surface fully coated with thorn-like Cu_xO nanostructures (Fig. 2a and b). HR-TEM images clearly indicated the crystal structure of the Cu_xO phase, in which the lattice fringes with d spacing of ~2.45 nm, 0.21 nm, and 0.274 nm correspond to the d(111) and d(200) crystal plane of Cu_2O, and d(110) crystal plane of CuO phase, respectively, indicating that Cu_xO has a polycrystalline nature with multi-crystal domains (Fig. 2c). At the same time, HAADF-STEM analysis reveals the relative position of the elements within the nanoneedle structure due to the atomic number (Z)-based contrast. In this regard, because of the difference in the electron penetration efficiency of Cu, Au, and Cu_xO phases, STEM image clearly shows that the grey Cu nanoneedle with diameter of around 100 nm is uniformly covered by a layer of very small Au nanostructures, which form faint shell with white dots homogeneously distributed on the grey Cu nanoneedle core (Fig. 2d). In addition, the growth of vertical Cu_xO nanothorns on Cu NW with the mean thickness of ~50 nm is also observed with light-grey color. Together with STEM, the EDS area color mapping indicates the formation of a unique core-shell nanostructure of Au–Cu@Cu_xO NWs (Fig. 2e–g). The detailed structure was also obtained from the EDS line profiles for a Au–Cu@Cu_xO NW (Fig. 2h–k), in which the Cu signal is primarily distributed at the core region, while the Au signal is mainly positioned at NW's surface to form an inner shell, which is coated by an outer shell of vertical Cu_xO thorns.

3.2. XRD, BET, and XPS analyses

Fig. 3a shows the typical XRD patterns of the Cu NWs and Au–Cu@Cu_xO NWs materials. In the case of Cu NWs, the diffraction peaks located at 2θ of 43.2°, 50.4°, and 74.1°, are corresponding to the crystalline lattices of the Cu metal (Elzey et al., 2011). The XRD pattern of the Au–Cu@Cu_xO NWs shows that in addition to the specific characteristics of Cu, other peaks appearing at 2θ of 32.5, 36.4, 38.6, 53.6, 57.8, 66.1, and 67.7° are relate to the d(110), d(002), d(111), d(020), d (202), d(11-3), and d(220) lattice of the CuO phase, respectively (Zhao et al., 2013). The formation of Cu_2O phases is also confirmed with the availability of specific peaks at 29.5, 35.5, 42.2, 48.9, 61.5, and 71.9°, consistent with d(110), d(111), d(200), d(220), d(221), and d(311) crystal plane, respectively. In particular, two small peaks at 45.8, and 63.6° are indexed as the d(200) and d(220) crystal plane of the fcc Au phase (Kar et al., 2014), further indicating the formation of

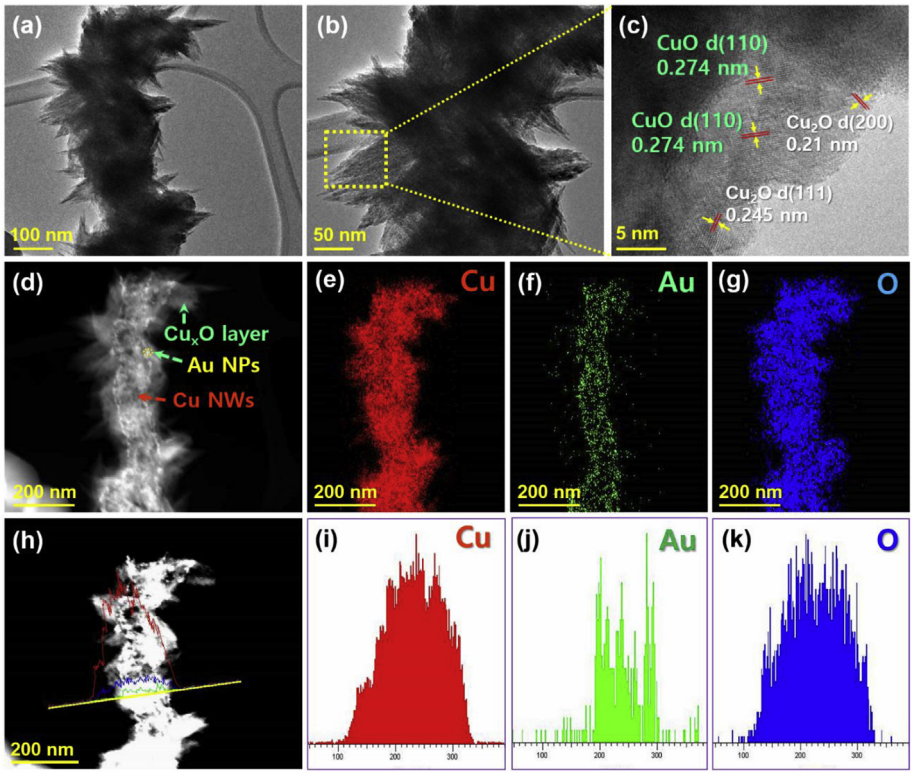

Fig. 2. (a and b) TEM and (c) HR-TEM images of the Au–Cu@Cu_xO NWs; (d) High contrast TEM images of the Au–Cu@Cu_xO NWs; EDS color mapping of the Au–Cu@Cu_xO NWs for (e) Cu, (f) Au, and (g) O; (h) STEM image of the Au–Cu@Cu_xO NWs along with line mapping profile of (i) Cu, (j) Au, (k) O.

Au–Cu@Cu_xO NWs nanoarchitecture.

The N_2 adsorption-desorption isotherms for studying the specific surface area and porosity of the materials are presented in Fig. 3b, which is discussed in detail in Supporting Information. The chemical composition of the Au–Cu@Cu_xO NWs material was further explored by XPS analysis. The survey XPS spectrum indicates the presence of binding energy for Cu2p, O1s, and Au4f at 934, 530, and 76 eV, respectively (Fig. 3c). The high resolution XPS spectrum of Cu2p shows three doublets, which are ascribed to binding energy of Cu^{2+}2p, Cu^{+}2p, and Cu^{o}2p at (932.8 and 952.7eV), (933.9 and 953.9 eV), and (935.2 and 955.2 eV), respectively, consistent with the presence CuO, Cu_2O, and Cu phase in Cu@Cu_xO NW structure (Fig. 3d). The appearance of satellite peaks for Cu^{2+}2p3/2 and Cu^{2+}2p1/2 at around 942 and 963 eV, respectively, further indicated the availability of CuO phase with the existence of an unfilled Cu3d^9 shell of Cu^{2+} (Jin et al., 2017). Fig. 3e shows the high resolution spectrum of O1s, which can be fitted by two peaks with binding energy at 529.7 and 531.1 eV, attributed to the Cu–O and adsorbed oxygen on surface of material, respectively (Devadoss et al., 2014). The high resolution spectrum of Au4f displays three separated components, in which the peaks at 83.6 and 87.2 eV are from Au^{o}4f, and the peak at 85.3 eV is from $Au^{\delta+}$4f (Fig. 3f) (Tchaplyguine et al., 2015). In order to observe the shifting of Cu2p and Au4f binding energies after hybridization, the XPS spectra of pure Cu NWs and Au nanoparticles were investigated (Figs. S2a and b). The shifting of the binding energy for Cu2p and Au4f is consistent with the charge transfer between two metallic phases, leading to the alternation of surface chemistry for each, including ionization energy and vacant-orbital numbers (Wong et al., 2017). These are important factors for Au–Cu interaction, because the creation of metallic bonding is resulted from the electrostatic appealing force between conduction electrons and positively charged metal ions. In this regard, Figs. S2c and d suggest a strong interaction between Au and Cu due to the significant shift of the Cu2p and Au4f binding energies in the hybrid as compared with pure Cu NWs and Au NPs. The positive shift of Au4f binding energy implies that the Au nanodots transfer electrons to the Cu@Cu_xO NWs, leading to the modulation of the d-band center in electronic structure of Au as well as Cu (Wong et al., 2017). The emergence of the prominent peaks of $Au^{\delta+}$ ions displays as advantageous electroactive sites and enhances the affinity between catalyst with reactant, thereby contributing the enhanced catalytic performance of hybrid in electrochemical reactions (Thanh et al., 2017).

3.3. Electrocatalytic properties towards L-cys oxidation

The electrocatalytic activity of the Au–Cu@Cu_xO NWs-3DF electrode was investigated for L-cys oxidation in 0.1 M PBS solution. A significant difference in the absence and presence of 1 mM L-cys is revealed from the CV measurement (Fig. 4a). In this regard, there is no peak current in blank PBS solution, whereas a clear peak appears at around +0.6 V in the presence of 1 mM L-cys, indicating the effective oxidation of such biomolecule on the electrode's surface. However, the disappearance of a reduction peak during cathodic scan implies the irreversible process of L-cys oxidation with a slow kinetic on the electrode's surface (Ge et al., 2012). The oxidation peak at the Au–Cu@Cu_xO NWs-3DF hybrid shows higher current along with negative potential as compared to those of bare 3DF, $Cu(OH)_2$ NWs-3DF, and Cu NWs-3DF (Fig. 4b). The superior performance of the Au–Cu@Cu_xO NWs-3DF is further supported by measuring amperometry at +0.6 V, in which its current response is around 2.65 mA, much higher than bare 3DF (0.83 mA), $Cu(OH)_2$ NWs-3DF (1.28 mA), and Cu NWs-3DF (2.05 mA) (Fig. 4c). The EIS was investigated to evaluate the charge transfer behavior at catalyst-electrolyte interface of different electrodes, since it is considered as a critical factor influencing on the catalytic behavior of the materials (Fig. 4d). In this context, the Au–Cu@Cu_xO NWs-3DF electrode exhibits a smaller semicircle at high frequency region as compared to other electrodes, suggesting a significant improvement of heterocharge transfer ability in its structure. This may be due to its hierarchical porous architecture with Au-integrated effect

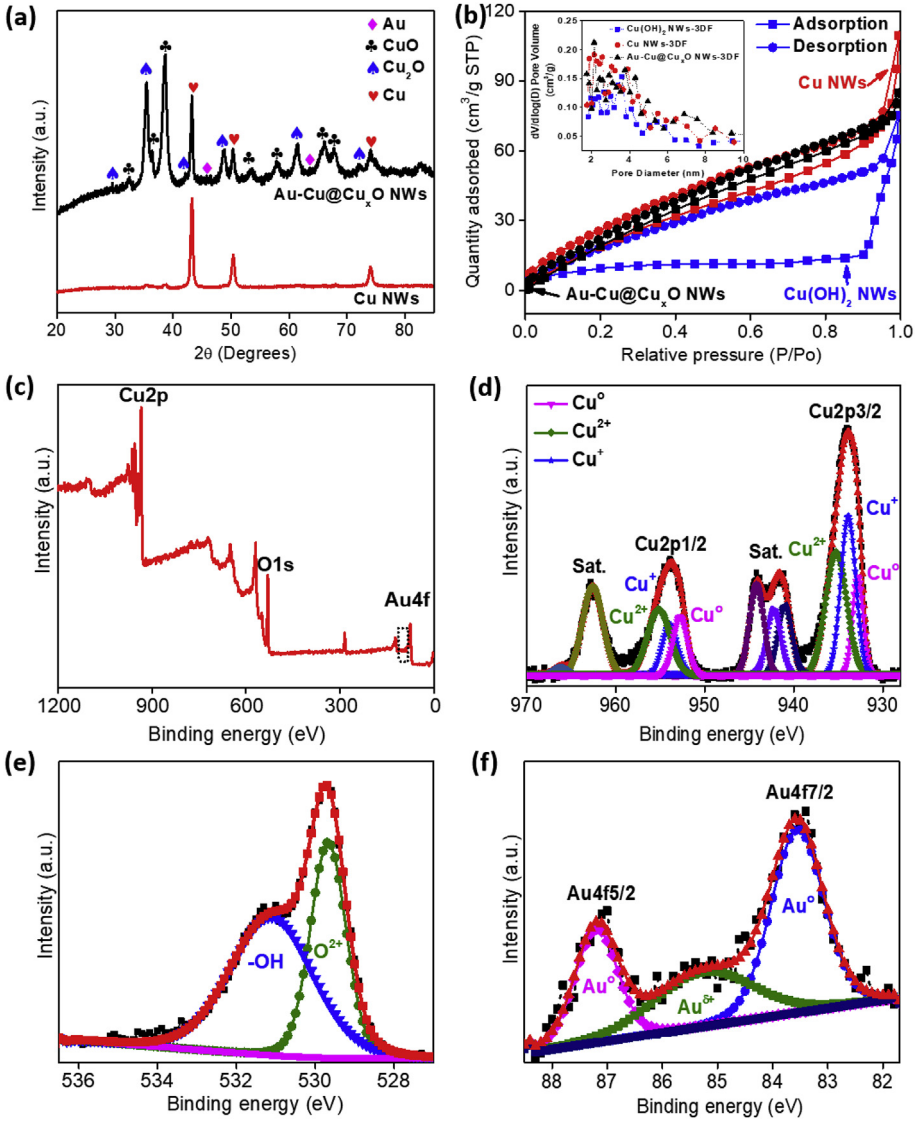

Fig. 3. (a) XRD patterns of the Au–Cu@Cu_xO NWs and Cu NWs materials; (b) BET surface area of $Cu(OH)_2$ NWs, Au–Cu@Cu_xO NWs and Cu NWs materials (inset: Pore distribution curves); (c) XPS spectrum of the Au–Cu@Cu_xO NWs; High resolution XPS spectra of (d) Cu2p, (e) O1s, and (f) Au4f in the hybrid material.

resulting in the improved charge transfer possibility. The enhanced catalytic performance of the Au–Cu@Cu_xO NWs-3DF electrode can be explained by some main reason as follow: Firstly, the combination of Au with Cu-Cu_xO nanoneedle significantly creates an alternation of the electronic properties for each other, thereby synergistically affecting the electroactive site number and charge conductivity of the resulting hybrid material. Secondly, the formation of a 3D hierarchical structure can offer the enhanced surface area with more exposed active sites, avoid undesirable interface, and reduce inner resistance by self-supported ability without using polymer binders and conductive additives. The high density of the macro- and mesopores easily endorse reactant/electrolyte accesses into the active sites of catalyst, thereby favorable for the fast charge transfer, reactant's adsorption, and ion/electrolyte penetration. At the same time, the growth of Cu NWs through a direct reaction of 3DF can lead to great adhesion to the substrate and ensure the good electrical contacts as well as mechanical behavior of the hybrid, further contributing its superior performance for long-term L-cys oxidation.

The kinetic of the L-cys oxidation on Au–Cu@Cu_xO NWs-3DF surface was investigated by CV at different potential scan rates (Fig. 4e). The results show that the current response is proportional to the square root of the scan rate with a linear equation of $I(mA) = 10.246V^{\frac{1}{2}} + 2.7761$ and a correlation coefficient (R^2) of 0.99069 (Inset in Fig. 4e), confirming that the L-cys oxidation at Au–Cu@Cu_xO NWs-3DF surface obeys a diffusion controlled process. The electrooxidation mechanism of L-cys can be proposed as the following equations (1)–(3) (Gao et al., 2005; Premlatha et al., 2018).

$$\text{Cu@Au@CuO-active site} + \text{RSH} \rightarrow \text{Cu@Au@CuO-active site}\cdots\text{RSH} \quad (1)$$

$$\text{Cu@Au@CuO-active site}\cdots\text{RSH} \rightarrow \text{Cu@Au@CuO-active site}\cdots\text{RS}^* + \text{H}^+ + \text{e}^- \quad (2)$$

$$2\text{Cu@Au@CuO-active site}\cdots\text{RS}^* \rightarrow 2\text{Cu@Au@CuO-active site} + \text{RS-SR} \quad (3)$$

(RSH = L-cys)

In another regard, to find the optimized value of the applied potential for L-cys detection, the influence of different applied potentials on the amperometric response of the Au–Cu@Cu_xO NWs-3DF electrode was investigated (Fig. 4f). The applied potential of + 0.6 V was found to produce the highest current response; therefore, it was chosen for subsequent amperometric experiments. The detection range, LOD, and sensitivity of the Au–Cu@Cu_xO NWs-3DF towards L-cys are explored by

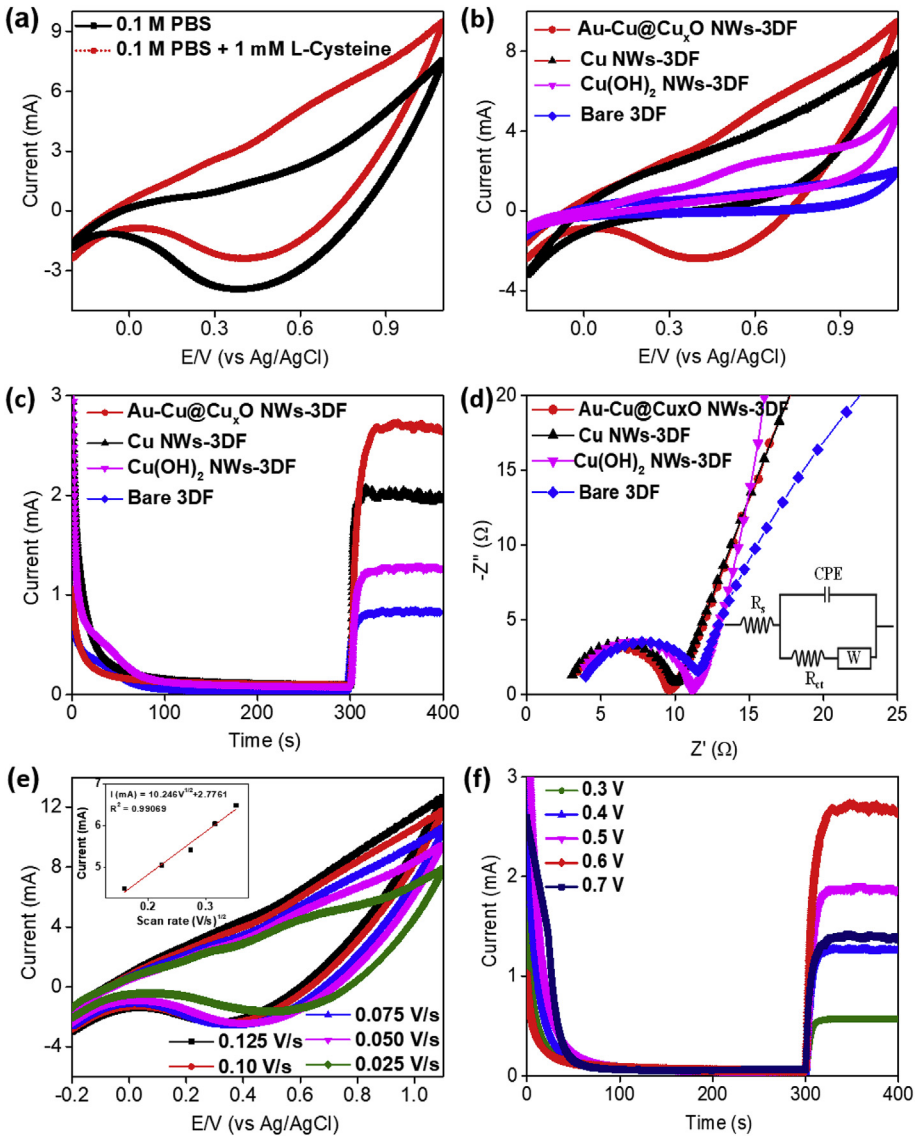

Fig. 4. (a) CV curves of Au–Cu@Cu$_x$O NWs-3DF in 0.1 M PBS solution, with and without 1 mM L-cys at a scan rate 50 mV/s; (b) CV curves of different electrodes in 0.1 M PBS solution containing 1 mM L-cys; (c) Amperometric curves of different electrodes in 0.1 M PBS solution containing 1 mM L-cys at an applied potential of +0.6 V; (d) EIS result of different electrodes in 0.1 M PBS solution containing 1 mM L-cys in the frequency range from 0.01 Hz to 10^5 Hz; (e) CV curves of Au–Cu@Cu$_x$O NWs-3DF in 0.1 M PBS solution + 1 mM L-cys at various scan rates; and (f) Amperometric curves of Au–Cu@Cu$_x$O NWs-3DF in 0.1 M PBS solution containing 1 mM L-cys at different applied potentials.

the amperometry through continuous addition of different L-cys concentrations into 0.1 M PBS solution (Fig. 5a). It was found that the Au–Cu@Cu$_x$O NWs-3DF displays an excellent sensitivity of 2945 μA cm^{-2} mM^{-1} to L-cys oxidation and a wide linear detection range from 1.25 μM to 1.94 mM, which is consistent with a regression equation of $I(mA) = 2.945C(mM) + 0.1733$ and a correlation coefficient (R^2) of 0.99877 (Fig. 5b). Besides, a low LOD value of 1.25 μM (S/N = 3) was realized (inset in Fig. 5a), along with a fast response time of 10 s (Fig. 5c). As compared with L-cys sensors reported in earlier studies (Table S1), the Au–Cu@Cu$_x$O NWs-3DF exhibits better behavior with regard to LOD, detection range, and sensitivity. Selectivity is also an important parameter for evaluating the practical potential of the sensor because the oxidation process of interferents may happen at a potential value similar to L-cys. To investigate the selectivity of the Au–Cu@Cu$_x$O NWs-3DF towards L-cys detection, the amperometry was carried out with an initial addition of 1 mM L-cys followed by subsequent addition of 0.05 mM DA, 0.05 mM KCl, 0.05 mM urea, 0.05 mM AA, 0.05 mM UA, and 0.5 mM L-cys. The concentration of these interferents is consistent with their level in the normal human body. Fig. 5c shows that mean L-cys with 1 mM and 0.5 mM at first time and final time of addition, respectively, shows an obviously sharp current increment; DA, KCl, urea, AA, and UA produce minor current responses in the 0.1 M PBS solution. The similar selective behavior of this sensor towards 1 mM L-cys detection in the presence of 0.5 mM glucose, 0.5 mM glycine, 0.5 mM H_2O_2, 0.5 mM citric acid, and 0.5 mM oxalic acid is also presented in Fig. S2, further indicating its excellent selectivity towards L-cys without influence of coexisting biomolecules. The reproducibility of the Au–Cu@Cu$_x$O NWs-3DF was examined by measuring the oxidation of 1 mM L-cys through five different electrodes (Fig. 5d). The relative standard deviation percentage (RSD%) was found to be 1.53%, suggesting that Au–Cu@Cu$_x$O NWs-3DF has excellent reproducibility. In another regard, the good stability of this sensor was also confirmed with a current retention of 94.6% over a period of four weeks stored (Fig. 5e). These results clearly indicate that the Au–Cu@Cu$_x$O NWs-3DF exhibits not only good catalytic activity but also respectable durability and stability for L-cys detection, highly potential for a practical application.

To prove the real application of the Au–Cu@Cu$_x$O NWs-3DF, a human serum sample was used for the L-cys detection. In a procedure, current intensity is achieved after injecting a certain amount of human serum into 0.1 mM PBS containing known L-cys concentration at the applied potential of +0.6 V. The accuracy of L-cys determination by Au–Cu@Cu$_x$O NWs-3DF in a human serum–spiked PBS solution was compared to the known value of L-cys concentration, as presented in Fig. 5f and Table S2. The recovery and RSD% values for detecting L-cys are found in the ranges of (101–109%) and (1.7–4.3%), respectively,

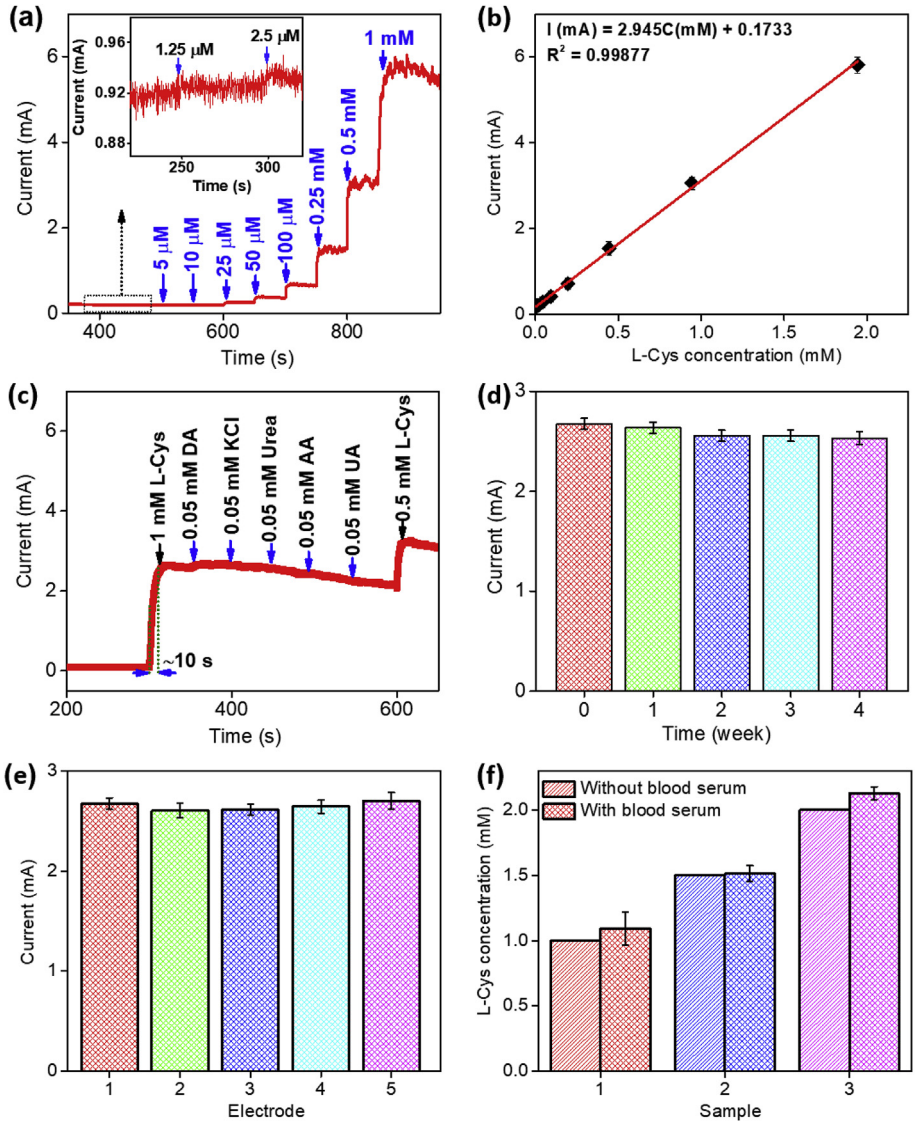

Fig. 5. The amperometric response of Au–Cu@Cu_xO NWs-3DF by adding various L-cys concentrations with regular intervals of 50 s at +0.6 V; (b) Effect of interferents on the performance of Au–Cu@Cu_xO NWs-3DF towards L-cys detection in 0.1 M PBS solution; (c) Amperometric current vs L-cys concentration; (d) Stability and (e) reproducibility of Au–Cu@Cu_xO NWs-3DF; (f) Practical application of Au–Cu@Cu_xO NWs-3DF for detecting known L-cys concentrations in blood serum spiked PBS solution.

demonstrating the suitable accuracy and good reliability of the Au–-Cu@Cu_xO NWs-3DF for nonenzymatic L-cys detection.

4. Conclusion

In this work, we successfully fabricated a novel porous hybrid of Au–Cu@Cu_xO NWs-3DF owning large electroactive surface area, excellent conductivity, and good stability. The hybrid exhibits a great advantage for L-cys detection with excellent sensitivity of 2945 μA cm^{-2} mM^{-1}, low LOD of 1.25 μM, and a wide linear detection range of 1.25 μM–1.94 mM. In addition to good reproducibility and stability, the hybrid also demonstrates the accurate detection of L-cys in real samples, implying its prospective ability towards practical sensing application. The enhanced sensing performance of the hybrid is due to the unique interaction between small Au and Cu to offer an intrinsic modulation of electronic properties and surface chemistry for each, which enhance electroactive site number and conductivity, thereby leading to a synergistic effect to accelerate the oxidation of L-cys. At the same time, the formation of a favorable hierarchical 3D nanoarchitecture with large surface area and high mechanical properties improves electrolyte penetration, ion diffusion, mass transfer, and charge transfer ability. The outstanding performance of the Au–Cu@Cu_xO NWs-3DF towards L-cys detection opens a novel door for developing effective self-supported catalyst in electrochemical sensing applications.

Declaration of interests

The authors declare that they have no known competing financial interests or personal relationships that could have appeared to influence the work reported in this paper.

CRediT authorship contribution statement

Huu Tuan Le: Methodology, Investigation, Validation, Formal analysis. **Duy Thanh Tran:** Methodology, Data curation, Writing - original draft, Visualization. **Thi Luu Luyen Doan:** Methodology, Investigation, Validation. **Nam Hoon Kim:** Conceptualization, Writing - review & editing, Supervision. **Joong Hee Lee:** Conceptualization, Writing - review & editing, Supervision, Project administration.

Acknowledgements

This research was supported by the Nano-Material Technology Development Program (2016M3A7B4900117), and Basic Science Research Program (2019R1A2C1004983) through the National Research Foundation (NRF) funded by the Ministry of Science and ICT of Republic of Korea.

Appendix A. Supplementary data

Supplementary data to this article can be found online at https://doi.org/10.1016/j.bios.2019.111327.

References

Abad, A., Concepción, P., Corma, A., García, H., 2005. A collaborative effect between gold and a support induces the selective oxidation of alcohols. Angew. Chem. Int. Ed. 44, 4066–4069. https://doi.org/10.1002/anie.200500382.

Billy, J.T., Co, A.C., 2018. Reducing the onset potential of CO2 electroreduction on CuRu bimetallic particles. Appl. Catal. B Environ. 237, 911–918. https://doi.org/10.1016/J.APCATB.2018.06.072.

Caldas, P.C.P., Gallo, J.M.R., Lopez-Castillo, A., Zanchet, D., Bueno, J.M.C., 2017. The structure of the Cu-CuO sites determines the catalytic activity of Cu nanoparticles. ACS Catal. 7, 2419–2424. https://doi.org/10.1021/acscatal.6b03642.

Deng, C., Chen, J., Chen, X., Wang, M., Nie, Z., Yao, S., 2009. Electrochemical detection of l-cysteine using a boron-doped carbon nanotube-modified electrode. Electrochim. Acta 54, 3298–3302. https://doi.org/10.1016/j.electacta.2008.12.045.

Devadoss, A., Sudhagar, P., Ravidhas, C., Hishinuma, R., Terashima, C., Nakata, K., Kondo, T., Shitanda, I., Yuasa, M., Fujishima, A., 2014. Simultaneous glucose sensing and biohydrogen evolution from direct photoelectrocatalytic glucose oxidation on robust Cu2O-TiO2 electrodes. Phys. Chem. Chem. Phys. 16, 21237–21242. https://doi.org/10.1039/c4cp03262d.

Eilert, A., Cavalca, F., Roberts, F.S., Osterwalder, J., Liu, C., Favaro, M., Crumlin, E.J., Ogasawara, H., Friebel, D., Pettersson, L.G.M., Nilsson, A., 2017. Subsurface oxygen in oxide-derived copper electrocatalysts for carbon dioxide reduction. J. Phys. Chem. Lett. 8, 285–290. https://doi.org/10.1021/acs.jpclett.6b02273.

Elzey, S., Baltrusaitis, J., Bian, S., Grassian, V.H., 2011. Formation of paratacamite nanomaterials via the conversion of aged and oxidized copper nanoparticles in hydrochloric acidic media. J. Mater. Chem. 21, 3162–3169. https://doi.org/10.1039/c0jm03705b.

Gao, Z.N., Yao, H.Q., Liu, W.Y., 2005. Study on electrocatalytic oxidation of L-cysteine at glassy carbon electrode by (FcM)TMA and its electrochemical kinetics. Electroanalysis 17, 619–624. https://doi.org/10.1002/elan.200403106.

Gawande, M.B., Pandey, R.K., Jayaram, R.V., 2012. Role of mixed metal oxides in catalysis science—versatile applications in organic synthesis. Catal. Sci. Technol. 2, 1113–1125. https://doi.org/10.1039/c2cy00490a.

Ge, S., Yan, M., Lu, J., Zhang, M., Yu, F., Yu, J., Song, X., Yu, S., 2012. Electrochemical biosensor based on graphene oxide-Au nanoclusters composites for l-cysteine analysis. Biosens. Bioelectron. 31, 49–54. https://doi.org/10.1016/j.bios.2011.09.038.

Ghanbari, K., Babaei, Z., 2016. Fabrication and characterization of non-enzymatic glucose sensor based on ternary NiO/CuO/polyaniline nanocomposite. Anal. Biochem. 498, 37–46. https://doi.org/10.1016/j.ab.2016.01.006.

Hassan, S.S.M., El-Baz, A.F., Abd-Rabboh, H.S.M., 2007. A novel potentiometric biosensor for selective l-cysteine determination using l-cysteine-desulfhydrase producing Trichosporon jirovecii yeast cells coupled with sulfide electrode. Anal. Chim. Acta 602, 108–113. https://doi.org/10.1016/j.aca.2007.09.007.

Huan, T.N., Rousse, G., Zanna, S., Lucas, I.T., Xu, X., Menguy, N., Mougel, V., Fontecave, M., 2017. A dendritic nanostructured copper oxide electrocatalyst for the oxygen evolution reaction. Angew. Chem. Int. Ed. 56, 4792–4796. https://doi.org/10.1002/anie.201700388.

Jana, S., Mondal, A., Ghosh, A., 2018. Fabrication of stable NiO/Fe2O3heterostructure: a versatile hybrid material for electrochemical sensing of glucose, methanol and enhanced photodecomposition and/photoreduction of water contaminants. Appl. Catal. B Environ. 232, 26–36. https://doi.org/10.1016/j.apcatb.2018.03.038.

Jason, N.N., Wang, S.J., Bhanushali, S., Cheng, W., 2016. Skin inspired fractal strain sensors using a copper nanowire and graphite microflake hybrid conductive network. Nanoscale 8, 16596–16605. https://doi.org/10.1039/c6nr04056j.

Jin, Z., Liu, C., Qi, K., Cui, X., 2017. Photo-reduced Cu/CuO nanoclusters on TiO 2 nanotube arrays as highly efficient and reusable catalyst. Sci. Rep. 7, 1–9. https://doi.org/10.1038/srep39695.

Kar, P., El-Tahlawy, M.K., Zhang, Y., Yassin, M., Mahdi, N., Kisslinger, R., Thakur, U.K., Askar, A.M., Fedosejevs, R., Shankar, K., 2017. Anodic copper oxide nanowire and nanopore arrays with mixed phase content: synthesis, characterization and optical limiting response. J. Phys. Commun. 1 045012. https://doi.org/10.1088/2399-6528/aa93a4.

Kar, P.K., Murmu, S., Saha, S., Tandon, V., Acharya, K., 2014. Anthelmintic efficacy of gold nanoparticles derived from a phytopathogenic fungus, Nigrospora oryzae. PLoS One 9, 1–9. https://doi.org/10.1371/journal.pone.0084693.

Karmaoui, M., Lajaunie, L., Tobaldi, D.M., Leonardi, G., Benbayer, C., Arenal, R., Labrincha, J.A., Neri, G., 2017. Modification of anatase using noble-metals (Au, Pt, Ag): toward a nano heterojunction exhibiting simultaneously photocatalytic activity and plasmonic gas sensing. Appl. Catal. B Environ. 218, 370–384. https://doi.org/10.1016/j.apcatb.2017.06.010.

Konar, S., Kalita, H., Puvvada, N., Tantubay, S., Mahto, M.K., Biswas, S., Pathak, A., 2016. Shape-dependent catalytic activity of CuO nanostructures. J. Catal. 336, 11–22. https://doi.org/10.1016/j.jcat.2015.12.017.

Li, J., Tang, H., Wang, Y., Huang, Z., Zhong, J., 2017. Thermally oxidation synthesis of CuO nanoneedles on Cu foam and its enhanced lithium storage performance. J. Mater. Sci. Mater. Electron. 28, 2353–2357. https://doi.org/10.1007/s10854-016-5803-8.

Liang, W., Fan, K., Luan, Y., Tan, Z., Al-Mamun, M., Wang, Y., Liu, P., Zhao, H., 2019. Sulfur-doped cobalt oxide nanowires as efficient electrocatalysts for iodine reduction reaction. J. Alloy. Comp. 772, 80–91. https://doi.org/10.1016/j.jallcom.2018.09.048.

Liu, X., Yang, W., Chen, L., Jia, J., 2017. Three-Dimensional copper foam supported CuO nanowire arrays: an efficient non-enzymatic glucose sensor. Electrochim. Acta 235, 519–526. https://doi.org/10.1016/j.electacta.2017.03.150.

Majd, S.M., Teymourian, H., Salimi, A., 2013. Fabrication of an electrochemical l-cysteine sensor based on graphene nanosheets decorated manganese oxide nanocomposite modified glassy carbon electrode. Electroanalysis 25, 2201–2210. https://doi.org/10.1002/elan.201300245.

Mierczynski, P., Vasilev, K., Mierczynska, A., Maniukiewicz, W., Szynkowska, M.I., Maniecki, T.P., 2016. Bimetallic Au-Cu, Au-Ni catalysts supported on MWCNTs for oxy-steam reforming of methanol. Appl. Catal. B Environ. 185, 281–294. https://doi.org/10.1016/j.apcatb.2015.11.047.

Mishra, A.K., Mukherjee, B., Kumar, A., Jarwal, D.K., Ratan, S., Kumar, C., Jit, S., 2019. Superficial fabrication of gold nanoparticles modified CuO nanowires electrode for non-enzymatic glucose detection. RSC Adv. 9, 1772–1781. https://doi.org/10.1039/C8RA07516F.

Momeni, M.M., Ghayeb, Y., Menati, M., 2016. Facile and green synthesis of CuO nanoneedles with high photo catalytic activity. J. Mater. Sci. Mater. Electron. 27, 9454–9460. https://doi.org/10.1007/s10854-016-4992-5.

Peng, H., Liu, Y., Guo, Y., Zhang, J., Zhang, L., Zhou, S., Xu, X., Liu, W., Zhang, N., Wang, X., 2016. Treating copper(II) oxide nanoflowers with hydrogen peroxide: a novel and facile strategy to prepare high-performance copper(II) oxide nanosheets with exposed (1 1 0) facets. ChemCatChem 8, 3714–3719. https://doi.org/10.1002/cctc.201601123.

Premlatha, S., Selvarani, K., Ramesh Bapu, G.N.K., 2018. Facile electrodeposition of hierarchical Co-Gd_2O_3 nanocomposites for highly selective and sensitive electrochemical sensing of L–cysteine. ChemistrySelect 3, 2665–2674. https://doi.org/10.1002/slct.201800012.

Ren, H., Huang, Z.H., Yang, Z., Tang, S., Kang, F., Lv, R., 2017. Facile synthesis of free-standing nickel chalcogenide electrodes for overall water splitting. J. Energy Chem. 26, 1217–1222. https://doi.org/10.1016/j.jechem.2017.10.004.

Silva, F., de, A., dos, S., da Silva, M.G.A., Lima, P.R., Meneghetti, M.R., Kubota, L.T., Goulart, M.O.F., 2013. A very low potential electrochemical detection of l-cysteine based on a glassy carbon electrode modified with multi-walled carbon nanotubes/gold nanorods. Biosens. Bioelectron. 50, 202–209. https://doi.org/10.1016/j.bios.2013.06.036.

Singh, M., Weerathunge, P., Liyanage, P.D., Mayes, E., Ramanathan, R., Bansal, V., 2017. Competitive inhibition of the enzyme-mimic activity of Gd-based nanorods toward highly specific colorimetric sensing of L-cysteine. Langmuir 33, 10006–10015. https://doi.org/10.1021/acs.langmuir.7b01926.

Sornambikai, S., Abdul Kadir, M.R., Kumar, A.S., Ponpandian, N., Viswanathan, C., 2017. Selective and low potential electrocatalytic oxidation and sensing of l-cysteine using metal impurity containing carbon black modified electrode. Anal. Methods 9, 6791–6800. https://doi.org/10.1039/c7ay02251d.

Tchaplyguine, M., Mikkelä, M.H., Zhang, C., Andersson, T., Björneholm, O., 2015. Gold oxide nanoparticles with variable gold oxidation state. J. Phys. Chem. C 119, 8937–8943. https://doi.org/10.1021/acs.jpcc.5b00811.

Thanh, T.D., Balamurugan, J., Hwang, J.Y., Kim, N.H., Lee, J.H., 2016. In situ synthesis of graphene-encapsulated gold nanoparticle hybrid electrodes for non-enzymatic glucose sensing. Carbon N. Y. 98, 90–98. https://doi.org/10.1016/j.carbon.2015.10.081.

Thanh, T.D., Balamurugan, J., Tuan, N.T., Jeong, H., Lee, S.H., Kim, N.H., Lee, J.H., 2017. Enhanced electrocatalytic performance of an ultrafine AuPt nanoalloy framework embedded in graphene towards epinephrine sensing. Biosens. Bioelectron. 89. https://doi.org/10.1016/j.bios.2016.09.076.

Thanh, T.D., Chuong, N.D., Hien, H. Van, Kim, N.H., Lee, J.H., 2018. CuAg@Ag core-shell nanostructure encapsulated by N-doped graphene as a high-performance catalyst for oxygen reduction reaction. ACS Appl. Mater. Interfaces 10, 4672–4681. https://doi.org/10.1021/acsami.7b16294.

Tran, D.T., Le, H.T., Luyen Doan, T.L., Kim, N.H., Lee, J.H., 2019. Pt nanodots monolayer modified mesoporous Cu@Cu x O nanowires for improved overall water splitting reactivity. Nano Energy 59, 216–228. https://doi.org/10.1016/j.nanoen.2019.02.050.

Ulrich, V., Froese, C., Moroz, B., Pyrjaev, P., Gerasimov, E., Sinev, I., Cuenya, B.R., Muhler, M., Bukhtiyarov, V., Grünert, W., 2018. Three-way catalysis with supported gold catalysts: poisoning effects of hydrocarbons. Appl. Catal. B Environ. 237, 1021–1032. https://doi.org/10.1016/j.apcatb.2018.06.063.

Wang, C., Yang, F., Cao, Y., He, X., Tang, Y., Li, Y., 2017. Cupric oxide nanowires on three-dimensional copper foam for application in click reaction. RSC Adv. 7, 9567–9572. https://doi.org/10.1039/C7RA00014F.

Wang, X., Ge, C. ye, Chen, K., Zhang, Y.X., 2018. An ultrasensitive non-enzymatic glucose sensors based on controlled petal-like CuO nanostructure. Electrochim. Acta 259, 225–232. https://doi.org/10.1016/j.electacta.2017.10.182.

Wang, X., Luo, C., Li, L., Duan, H., 2015. Highly selective and sensitive electrochemical

sensor for l-cysteine detection based on graphene oxide/multiwalled carbon nanotube/manganese dioxide/gold nanoparticles composite. J. Electroanal. Chem. 757, 100–106. https://doi.org/10.1016/j.jelechem.2015.09.023.

Wong, R.J., Scott, J., Kappen, P., Low, G.K.C., Hart, J.N., Amal, R., 2017. Enhancing bimetallic synergy with light: the effect of UV light pre-treatment on catalytic oxygen activation by bimetallic Au-Pt nanoparticles on a TiO2 support. Catal. Sci. Technol. 7, 4792–4805. https://doi.org/10.1039/c7cy01326d.

Yang, Jie, Hu, J., Weng, M., Tan, R., Tian, L., Yang, Jinlong, Amine, J., Zheng, J., Chen, H., Pan, F., 2017. Fe-cluster pushing electrons to N-doped graphitic layers with Fe3C(Fe) hybrid nanostructure to enhance O2 reduction catalysis of Zn-air batteries. ACS Appl. Mater. Interfaces 9, 4587–4596. https://doi.org/10.1021/acsami.6b13166.

Yu, T., Zeng, J., Lim, B., Xia, Y., 2010. Aqueous-phase synthesis of Pt/CeO2 hybrid nanostructures and their catalytic properties. Adv. Mater. 22, 5188–5192. https://doi.org/10.1002/adma.201002763.

Zhao, B., Liu, P., Zhuang, H., Jiao, Z., Fang, T., Xu, W., Lu, B., Jiang, Y., 2013. Hierarchical self-assembly of microscale leaf-like CuO on graphene sheets for high-performance electrochemical capacitors. J. Mater. Chem. 1, 367–373. https://doi.org/10.1039/c2ta00084a.

Zhao, S., Jin, Renxi, Abroshan, H., Zeng, C., Zhang, H., House, S.D., Gottlieb, E., Kim, H.J., Yang, J.C., Jin, Rongchao, 2017. Gold nanoclusters promote electrocatalytic water oxidation at the nanocluster/$CoSe_2$ interface. J. Am. Chem. Soc. 139, 1077–1080. https://doi.org/10.1021/jacs.6b12529.

Zhou, M., Ding, J., Guo, L.P., Shang, Q.K., 2007. Electrochemical behavior of L-cysteine and its detection at ordered mesoporous carbon-modified glassy carbon electrode. Anal. Chem. 79, 5328–5335. https://doi.org/10.1021/ac0703707.